Subtropical jet regulates Arabian winter precipitation: a viable mechanism

Subtropical Jet Regulates Arabian Winter Precipitation: A Viable Mechanism

SOURAV TARAPHDAR,[a,b] DEEPAK GOPALAKRISHNAN,[a,c] CHANGHAI LIU,[d] OLIVIER M. PAULUIS,[a,e] LULIN XUE,[d,f] R. S. AJAYAMOHAN,[a,g] L. RUBY LEUNG,[b] SAMSON HAGOS,[b] WOJCIECH W. GRABOWSKI,[d] SISI CHEN,[d] ROY M. RASMUSSEN,[d] AND SARAH A. TESSENDORF[d]

[a] *Arabian Center for Climate and Environmental Sciences, New York University Abu Dhabi, Abu Dhabi, United Arab Emirates*
[b] *Pacific Northwest National Laboratory, Richland, Washington*
[c] *Central Michigan University, Mount Pleasant, Michigan*
[d] *National Center for Atmospheric Research, Boulder, Colorado*
[e] *Courant Institute of Mathematical Science, New York University, New York, New York*
[f] *Hua Xin Chuang Zhi Science and Technology LLC, Beijing, China*
[g] *Department of Geography, Ohio University, Athens, Ohio*

(Manuscript received 23 October 2023, in final form 10 October 2024, accepted 13 January 2025)

ABSTRACT: The present study explores the mechanism governing wintertime (November–April) precipitation over the Arabian Peninsula (AP) using a 17-yr-long (2002–18) high-resolution WRF simulation. The composite analysis of strong precipitation events suggests that the equatorward extension of the upper-level jet together with the embedded upper-level trough creates a positive (cyclonic) midlevel vorticity and subsequently generates an anomalous lower-level convergence through Ekman pumping. This leads to the development of an anomalous surface low, which is further enhanced in the presence of the existing Red Sea trough over the AP. This surface low weakens the persistent anticyclone over the AP, shifting it further eastward to the Arabian Sea. The eastward shift in the lower-level anticyclone contributes to the transport of warm, moist air from the Arabian Sea and the Red Sea toward the AP. This warm, moist air converges with the cold and dry air advected by the midlatitude jet and creates a moisture convergence zone, leading to the initiation of convection. We test the proposed mechanism through numerical experiments with modified upper-level wind and demonstrate that a strong, southward intrusion of the jet can indeed lead to precipitation over the AP. The above mechanism also explains the interannual variability of precipitation over the AP. During wet years, we notice approximately 3 m s^{-1} stronger jet core magnitude and about a 2° equatorward shift of the jet compared to dry years. While the equatorward extension of the jet explains about 21% of the interannual variability, the jet magnitude explains around 7% of the variability during wet years.

SIGNIFICANCE STATEMENT: Understanding the mechanism governing rainfall variability is crucial for the arid Arabian Peninsula. We conducted 17-yr (2002–18) high-resolution simulations using the WRF Model to understand the rainfall variability and the model's ability to capture rainfall patterns. We propose a mechanism behind winter–spring (November–April) season precipitation over the Arabian region and its connections with the subtropical jet. The results reveal that an equatorward shift of the jet is associated with above-normal rainfall over the Arabian Peninsula. Our study has identified a new pathway through which the subtropical jet's location influences rainfall patterns over this region. This finding assumes significant importance, especially considering the anticipated changes in the subtropical jet's position in a warmer climate.

KEYWORDS: Jets; Precipitation; Regional models; Interannual variability

1. Introduction

The Arabian regional climate consists of various landscapes, from high orography (Zagros Mountains) in the north to the interior's vast arid lands, including the dunes. It is also surrounded by several water bodies (Red Sea, Arabian Sea, and the Arabian Gulf). While the climate of the Arabian Peninsula (AP) is characterized by high temperatures and low precipitation amounts, annual cycles remain pronounced, with maximum winter precipitation (November–April) and minimum summer (May–October) rainfall. Previous studies have noted that wintertime precipitation is much stronger than summer season precipitation and covers most of the Middle East regions (e.g., Almazroui et al. 2012; Taraphdar et al. 2021). The primary precipitation band in winter lies over the Zagros Mountains, extending to the AP. The mountainous regions typically receive more precipitation than low-elevation barren areas. The winter precipitation is mainly modulated by the synoptic-scale systems from the Mediterranean (Kumar et al. 2015; de Vries et al. 2016, 2018; Patlakas et al. 2019; Tuel et al. 2022).

Denotes content that is immediately available upon publication as open access.

Supplemental information related to this paper is available at the Journals Online website: https://doi.org/10.1175/JAS-D-23-0213.s1.

Corresponding author: Sourav Taraphdar, sourav.taraphdar@pnnl.gov, st113@nyu.edu

DOI: 10.1175/JAS-D-23-0213.1

High-resolution regional climate modeling studies focusing on the AP are limited to understanding the precipitation distributions and variabilities over the region. Studies related to the sensitivity of domain size, physical parameterizations, and regional boundary forcing in current climate conditions, followed by downscaling of temperature and precipitation in the present and future climate, have been performed over the AP using the RegCM4 model at about 50-km horizontal grid spacing (Almazroui 2011, 2012, 2016). While this resolution might be adequate to capture the large-scale dynamical features, finer grid spacing is needed to understand the detailed small-scale precipitation distribution or to resolve the precipitation processes (Evans et al. 2004; Jing et al. 2017). With the improvement in computational power, higher resolution event-based (Gopalakrishnan et al. 2023; Francis et al. 2021; Armon et al. 2020; Fonseca et al. 2020; Schwitalla et al. 2020) and regional climate simulations over the AP (Hussain and Broeke 2015; Patlakas et al. 2019; Attada et al. 2020; Jing et al. 2020; Taraphdar et al. 2021; Attada et al. 2022) have been performed in recent years.

Sensitivity experiments on the impact of different cumulus parameterization schemes on simulating winter precipitation events over the AP found that the Kain–Fritsch scheme outperforms other schemes (Attada et al. 2020, 2022). However, convection-permitting models that explicitly resolve deep convection without using convective parameterizations have the advantage of avoiding error-prone convection parameterizations (Liu et al. 2017; Jing et al. 2017; Wang et al. 2018; Rasmussen et al. 2020). Jing et al. (2020) demonstrated the improved skill of convection-permitting (grid spacing of 5 km or finer) models over coarser-grid regional models in the Middle East region. However, convection-permitting simulations are computationally expensive for large domains and for long simulation periods; hence, they might only be affordable for a few climate research communities.

In atmospheric models, horizontal grid spacing between 3 and 10 km is referred to as gray-zone resolution (Pauluis and Garner 2006; Taraphdar et al. 2014; Chen et al. 2018; Taraphdar et al. 2021; Taraphdar and Pauluis 2021). Using the Weather Research and Forecasting (WRF) Model, Taraphdar et al. (2021) demonstrated that a gray-zone resolution model (horizontal grid length of 9 km) can achieve comparable skill to a convection-permitting model by choosing suitable model physics packages for the synoptic- and mesoscale precipitation, specifically for winter season precipitation. They performed several single-year-long simulations with different configurations of the WRF Model over the Middle East in general and the United Arab Emirates specifically to evaluate the model's ability to capture temporal and spatial distributions of precipitation. In the current study, we extend Taraphdar et al. (2021) to the analysis of a 17-yr-long WRF simulation in current climate conditions to understand its merit and limitation of gray-zone resolution before starting the future climate simulation.

Further, we also aim to understand the governing mechanism behind the winter season precipitation in the AP. The AP is located at the intersection of the tropics and midlatitude regions, making it an ideal testbed for studying tropics–midlatitude interactions. An important circulation feature connecting the tropics and midlatitudes is the westerly jet stream (Wei et al. 2017). Westerly jet streams are upper-level circulation systems in the midlatitude, and they provide unstable environments due to their intense horizontal and vertical wind shears (Held 1975; Li and Wettstein 2012). During boreal winter, three subtropical jet cores exist in the extratropical westerlies in the Northern Hemisphere (Wei et al. 2022). The Middle East jet stream (MEJS) is a prominent branch of the subtropical jet stream with its center located north of the AP at about 30°N (Wei et al. 2022; Ren et al. 2022). A stronger and southeastward-shifted MEJS (hereafter jet stream) relative to the climatological condition frequently allows European cold air to intrude into the Middle East region, promoting the occurrence and intensification of precipitation therein (de Vries et al. 2018; Atif et al. 2020).

Several past studies have investigated wintertime precipitation patterns across the Middle East region and have highlighted the importance of the interaction between midlatitude and tropical systems as a facilitating factor for these precipitation events (de Vries et al. 2013; Kumar et al. 2015; de Vries et al. 2016, 2018; Saeed and Almazroui 2019; Al-Nassar et al. 2020; Atif et al. 2020; Horan et al. 2023). A southward shift in the upper-level jet was also found to be favorable for enhanced wintertime rainfall (Kumar et al. 2016; Sandeep and Ajayamohan 2018) and dust storms (Alsubhi et al. 2023) over the AP. Kumar et al. (2015) examined an ensemble of extreme events over the central AP and found that, associated with potential vorticity intrusions, moisture buildup starts on average 8 days before the heavy rainfall event. They also noted cyclonic wind anomalies in the upper and lower levels, which they attributed to Rossby wave propagation. de Vries et al. (2016) examined three extreme rainfall events in the AP, showing that those events were initiated by midlatitude forcing through an upper-level trough intrusion into low latitudes. They also argued that tropical–extratropical interactions facilitated the moisture transport to the AP. A few previous studies have investigated the role of circumglobal wave trains on extreme rainfall events in the AP (e.g., Saeed and Almazroui 2019; Atif et al. 2020). For example, Atif et al. (2020) observed that a wave-like circumglobal wave train pattern enhances midlevel cyclonic activity and favors upper-level divergence through the jet stream. Further, anomalous low pressure in the lower troposphere over Saudi helps bring in warm, moist air from the Red Sea and the Arabian Sea, leading to extreme events. Alizadeh et al. (2021) analyzed the upper-tropospheric Rossby wave activity and its role in precipitation over the AP on a monthly time scale. They observed an above-normal Rossby wave activity over the Red Sea region in wetter months. Moreover, the Red Sea trough (RST) extended northward during this period, contributing to the rainfall occurrence and enhancement in the eastern Mediterranean, northeast Red Sea, and some parts of Saudi Arabia.

Several studies have identified the crucial role of the interaction between tropical and extratropical systems in the genesis of wintertime rainfall events in the AP and reported that the moisture required for these types of rainfall events is generally transported from the Red Sea and the Arabian Sea. However, a complete picture of the entire chain of events leading to wintertime precipitation events in the region is still not clear.

Moreover, the relative contribution of the strength and position of the jet stream have not been clearly quantified.

This study is part of an overarching project to develop an efficient regional climate model for the AP that realistically captures the winter season precipitation distributions. Working toward this goal, we address two specific objectives in this study: (i) to understand the biases in high-resolution WRF for regional climate model applications over the AP and (ii) to advance our knowledge of the role of the jet streams in wintertime precipitation events in the AP. Unlike most of the previous studies, which have primarily focused on diagnostic analyses, we aim to test our hypothesis and demonstrate the causal relationship of jet streams to rainfall using numerical experiments. We also explore whether the proposed mechanism can explain the interannual variability in wintertime precipitation over the AP.

2. Numerical design, methodology, and verifications

a. Model configurations

The nonhydrostatic WRF Model, version 4.1.2 (Skamarock et al. 2019), is used in the present study with a single model domain (481 × 361 grid points) covering 7.5°–39°N and 30°–78°E (Fig. 1) at 9-km horizontal grid spacing. There are 45 stretched vertical levels from the surface to the model top at 10 hPa. Taraphdar et al. (2021) identified the model's horizontal and vertical resolution through a series of sensitivity experiments, and the best configuration is used in the current manuscript. This domain extends over the AP and the central part of the Arabian Sea, part of western India in the east, and part of eastern Africa in the far west. We have tested three subregions of different sizes over the domain to quantify the model's performance against observations or reanalysis. The black box (20° × 20°; region 1) in Fig. 1 covers the major precipitation distribution over the Middle East area (40°–60°E and 17°–37°N), including part of the Zagros Mountains, the Arabian Gulf, and also part of the Arabian Desert. Region 2 (red box; 20° × 10°) covers most of the AP (40°–60°E and 17°–27°N), excluding the Zagros Mountains. The third box (5° × 4°; region 3) mainly covers the United Arab Emirates, including part of the coastal Arabian Gulf (52°–57°E and 23°–26°N), the region of our interest.

The physical parameterizations used in the current study follow Taraphdar et al. (2021), the best suitable configuration over this region. The cloud microphysical processes are parameterized by the aerosol-aware Thompson–Eidhammer scheme (Thompson and Eidhammer 2014). This scheme has six classes of hydrometeors and uses a double-moment representation for warm rain. The boundary layer is parameterized by the quasi-normal scale elimination (QNSE) scheme (Sukoriansky et al. 2005), a local closure scheme that includes turbulent kinetic energy as a prognostic variable. The QNSE PBL is tied to its surface layer scheme. The Noah land surface model with multiparameterization options (Noah-MP) (Niu et al. 2011) represents land surface processes and land–atmosphere interaction. Atmospheric radiative heating is calculated by the Rapid Radiative Transfer Model (Iacono et al. 2011) schemes for longwave and shortwave radiation. Our model configuration does not use any parameterization for deep convection but depends on the resolved dynamics to capture the impact of convective activity (Pauluis and Garner 2006; Satoh et al. 2014; Taraphdar and Pauluis 2021; Taraphdar et al. 2021).

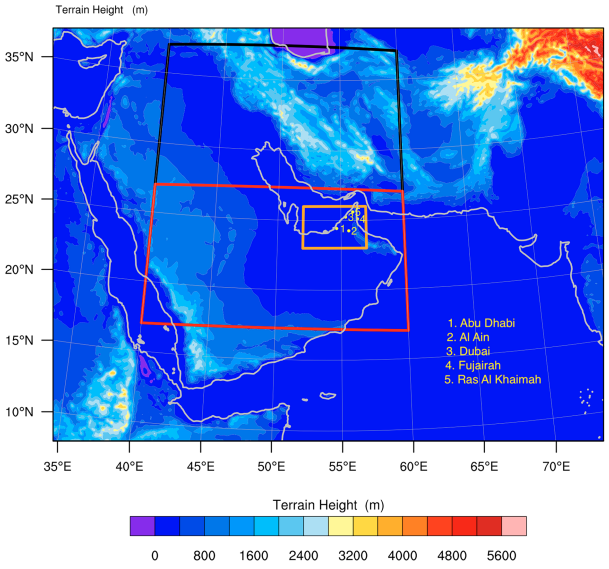

FIG. 1. The model domain with underlying terrain heights (m; shaded). The black box indicates a large area over the Middle East region (region 1: 40°–60°E and 17°–37°N), while the red box (region 2: 40°–60°E and 17°–27°N) depicts mostly the AP and the orange box covers mostly the United Arab Emirates and surroundings (region 3: 52°–57°E and 23°–26°N). Five station observation sites from the National Center for Meteorology (NCM) at the United Arab Emirates are shown by the numbers one to five within the orange box.

The lateral boundary and the sea surface temperature are updated every 3 h using ERA5 reanalysis at around 31-km horizontal grid length (Hersbach et al. 2020). The WRF simulation was initialized at 0000 UTC 1 January 2002 and integrated for 17 years ending at 0000 UTC 1 January 2019 to capture the interannual evolutions. Spectral nudging is used for the first 5 days only to relax the horizontal wind with a meridional wavenumber 0–2 and zonal wavenumber 0–4 to constrain the large-scale flow and convergence in the domain and to allow for the mesoscale to saturate in the spectral space (Zhang et al. 2017; Taraphdar et al. 2021).

b. Model evaluation and observational datasets

For comparison and evaluation of our experiments, we used 3-hourly observed rainfall from the Tropical Rainfall Measuring Mission (TRMM) 3B42, version 7, and Climate Hazards Group Infrared Precipitation with Station (CHIRPS-2.0; Funk et al. 2015) data, and ERA5 reanalysis for circulation, temperature, and moisture fields. The TRMM 3B42 dataset provides 3-hourly precipitation at a grid resolution of 0.25° × 0.25°. The TRMM dataset may underestimate light rainfall contributions, as earlier studies suggested (Iguchi et al. 2000; Schumacher and Houze 2000; Nesbitt and Zipser 2003). However, TRMM 3B42, V7, outperformed its predecessors when compared against observed rain gauge data over arid environments (Milewski et al. 2015),

being the best long-term observational precipitation estimate for evaluating the precipitation in the Arabian Gulf region according to Wehbe et al. (2018).

The CHIRPS dataset builds on previous approaches of "smart" interpolation techniques and high-resolution long period of record precipitation estimates based on infrared cold cloud duration (CCD) observations (Willmott and Matsuura 1995). The algorithm builds a 0.05° climatology incorporating satellite information to represent sparsely gauged locations. It includes daily, pentad, and monthly 1981–the present 0.05° CCD-based precipitation estimates and blends station data to reproduce a preliminary information product with a latency of about 2 days and a final product with an average latency of about 3 weeks. This product is available for precipitation estimates at the highest spatial resolution (about 5 km) but only over land.

Six rain gauge station data from major airports in the United Arab Emirates are available for model evaluation (see Fig. 1). However, we used data only from five stations since there is a quality issue with the Sharjah station data specifically for lighter rain rates. Although the rain gauge datasets are available only for five stations, they reflect the spatial variability and provide ground truth for precipitation evaluation because of their higher accuracy than satellite retrievals (Liu et al. 2017), particularly in the case of the Arabian Gulf region (Wehbe et al. 2017). Besides comparing and evaluating our simulation with observations, we also analyzed the dynamical (e.g., moisture convergence, moist static energy, etc.) and thermodynamical (e.g., temperature, precipitable water, cloud fraction, etc.) diagnostics in detail to understand the model biases with respect to reanalysis.

c. *Methodology*

1) IDENTIFICATION OF PRECIPITATION EVENTS OVER THE AP

We first computed a daily time series of precipitation over the AP (40°–60°E and 17°E–27°N) during the winter season (November–April) for the 2002–18 period. Figure S1A in the online supplemental material shows an example for the season from November 2003 to April 2004. The red dashed line indicates the winter season mean precipitation averaged over the 17-yr period. We identified the event when the precipitation was higher than the winter season mean values and persisted for at least 3 days. From Fig. S1A, one can identify four precipitation events; out of them, two events are very strong (early December and late April). Similar procedure is applied for all 17 years and to the TRMM 3B42 data and WRF Model outputs. It is also clear that the events are well separated from each other. Following the above procedure, we identified 73 (68) winter season precipitation events from WRF output (TRMM 3B42) for the 17-yr period. We also changed the threshold from 3 to 5 days, resulting in a reduction of event to 43 (40) in WRF (TRMM 3B42) precipitation, respectively. Nonetheless, the results remain consistent and emphasize only the stronger events.

2) IDENTIFICATION OF UPPER-LEVEL JET

The daily wind magnitudes averaged between 400 and 100 hPa over the AP (40°–60°E) during the winter season (i.e., November–April) are calculated first. This gives a time series of jet magnitudes for all 17 years, which is then averaged to obtain the 17-yr mean climatological jet profile as a function of latitude (Fig. S1B). From the climatological jet profile, the magnitude of the jet core and the corresponding latitude are determined. Additionally, the standard deviation of the jet core location is computed from the daily jet profiles for 17 years. The northern and southern limits are then defined as ± 1 standard deviation of the climatological jet locations, respectively. The red (blue) dashed line in Fig. S1B shows the jet southern (northern) extension, respectively. The jet width is estimated as the distance between the southern and the northern extensions of the jet. Further, the daily values of jet magnitude, jet locations, jet width, and jet boundaries are converted to pentad data for the 17-yr winter periods.

3) IDENTIFICATION OF WET AND DRY YEARS OF PRECIPITATION OVER THE AP

The normalized precipitation anomaly over the AP is computed to identify the wet and dry years. First, the area (40°–60°E and 17°E–27°N) and time (winter season) averaged precipitation are calculated for each year from 2002 to 2018 and the climatology for these 17 years. Since the interannual evolution of rain in WRF, TRMM 3B42, and CHRIPS is highly correlated, stronger and weaker precipitation years are similar between the two observations and the WRF simulation. Further, the normalized anomaly (with respect to standard deviation) for each year is computed relative to its climatology. This gives a series of normalized precipitation anomalies, and years with values higher/lower than $+1/-1$ standard deviation signify wet and dry years, respectively.

3. Results and discussion

a. *Climatological mean and intraseasonal distribution of precipitation and circulation*

The annual averaged climatological (2002–18) precipitation distribution from TRMM 3B42, CHIRPS, and WRF simulation is compared in Fig. 2. The spatial distributions of precipitation are very similar in the observational products. WRF can capture the spatial pattern of rainfall in agreement with both observations. The primary precipitation band is over the Zagros Mountains, presumably associated with orographic enhancement, and extends over the Arabian Gulf, Saudi Arabia, and the United Arab Emirates. Compared to both observations, WRF overestimates the orographic rain (Figs. S2A,C) and is closer to the observations in the rest of the domain, specifically over the United Arab Emirates. The percentage departures of WRF precipitation from observations are pronounced (Figs. S2B,D), revealing more detailed structures over low-elevation areas. In general, AP shows a mix of positive and negative percentage departures. Specifically, the topographical regions have larger positive deviation compared to low-elevation areas. Similar findings are also noticed in the UAE regions, where the eastern part of the country (Al Hajar Mountain regions) suffers substantial wet biases (Figs. S2B,D).

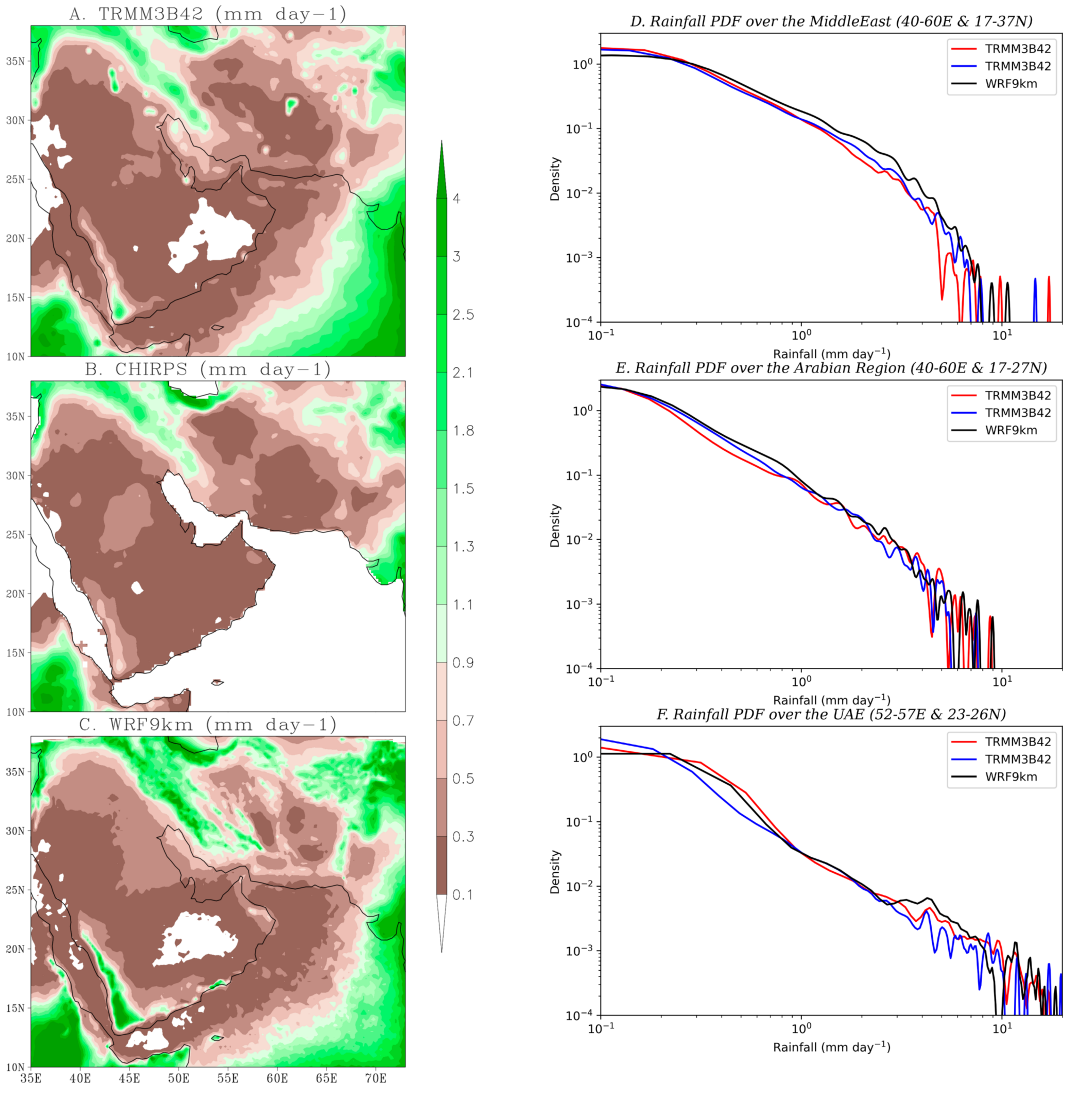

FIG. 2. The spatial distribution of annual averaged precipitation (mm day^{-1}) from (a) TRMM 3B42 observation, (b) CHIRPS observation, and (c) the WRF simulations at 9-km resolution. The probability distribution of precipitation over (d) region 1 (Middle East), (e) region 2 (AP), and (f) region 3 (UAE).

To quantify the WRF precipitation with respect to the different observations, the probability distribution function (PDF) of averaged daily rainfall is computed over the three regions. Figure 2d shows that WRF systematically overestimates the precipitation in all categories greater than 0.2 mm day^{-1} over the Middle East region and agrees with the wet biases over Zagros Mountains (Figs. S2A,C). The WRF Model performs relatively better over region 2 (AP), showing marginal overestimation of light rain below 1 mm day^{-1} (Fig. 2e). However, it offers a very similar pattern to observations in higher rain-rate categories (>1 mm day^{-1}). Model performance improves over region 3 (i.e., United Arab Emirates), indicating that WRF rainfall closely follows TRMM 3B42 and CHIRPS observations in almost all the precipitation categories (Fig. 2f). This improvement in WRF precipitation in all categories is likely due to the cancellation of wet biases over land and dry biases over the ocean in region 3 (Fig. S2B). We note that the difference in precipitation PDF between the two observation datasets is probably due to the unavailability of CHIRPS data over the oceanic region. Consistent with the precipitation PDF, annual average rainfall over the three regions suggests wet biases in WRF over region 1 (i.e., 63.7 and 60 mm yr^{-1} compared to TRMM and CHIRPS; Fig. 3a). The annual precipitation biases are reduced for the UAE regions (Figs. 3b,c). Over the United Arab Emirates, mean annual rainfall for the 17 years is highly consistent between TRMM 3B42 and WRF (TRMM = 92.56 mm yr^{-1}; WRF = 88.47 mm yr^{-1}) but somewhat differs from CHIRPS (70.56 mm yr^{-1}) possibly because of the unavailability of precipitation data over the oceanic regions. The monthly rainfall (Fig. 3) displays a distinct seasonality for all three regions, with more rain from November to April (wet/winter season) and less rain from May to October (dry/summer

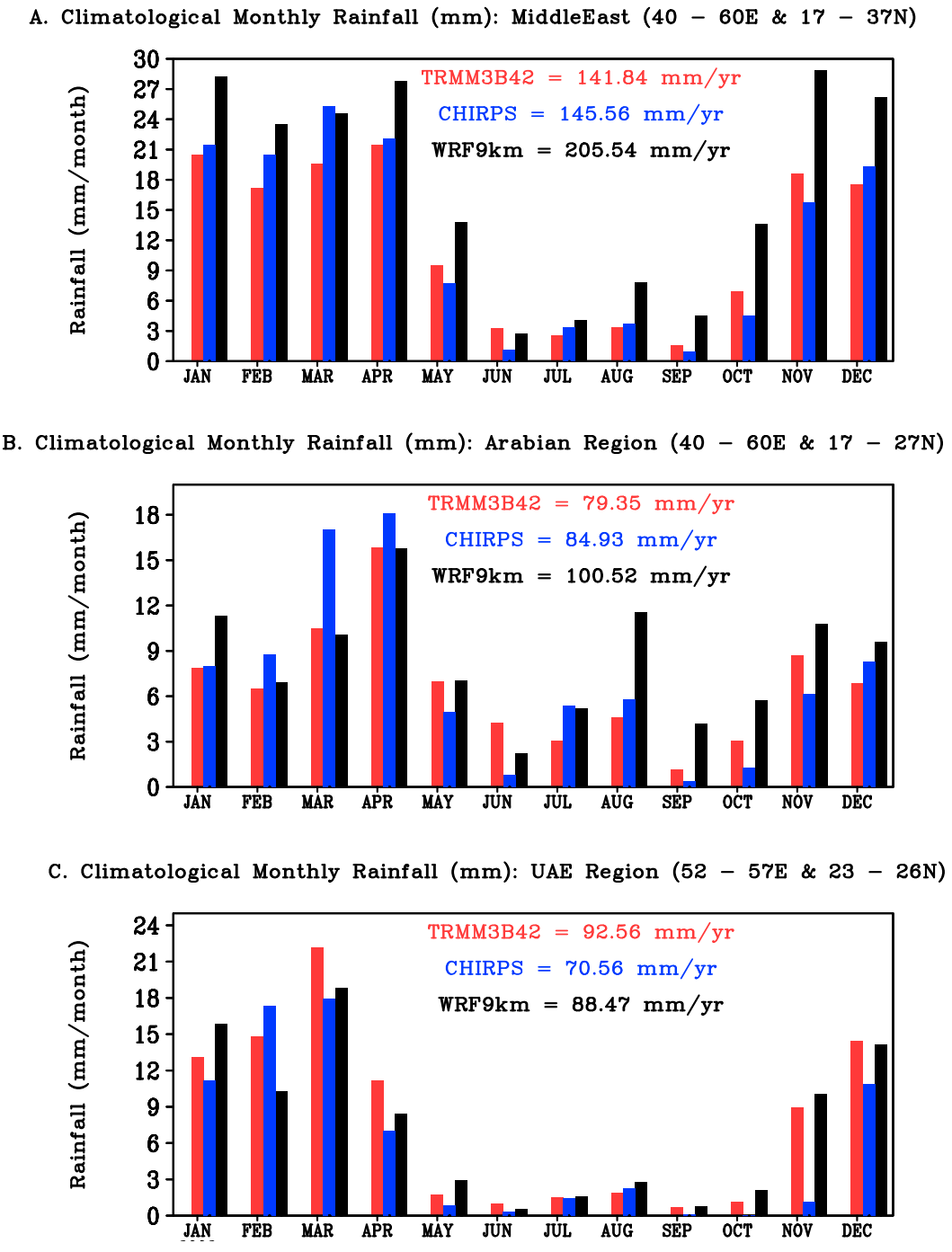

FIG. 3. (a) The climatological (2002–18) monthly precipitation (mm month^{-1}) over the Middle East region (40°–60°E and 17°–37°N). (b),(c) As in (a), but over the AP (40°–60°E and 17°–27°N) and the UAE region (52°–57°E and 23°–26°N), respectively.

season). WRF realistically captures this seasonality with some notable biases.

WRF performance relative to the five rain gauge observations across the United Arab Emirates was further analyzed. The annual precipitation is mainly dominated by the winter season, and WRF has wet biases in all the station locations (figure not shown). To identify the precipitation categories responsible for these annual biases, we computed the WRF rainfall PDF at each station location and compared it with the rain gauge data and TRMM 3B42 (Fig. 4). The rain gauge data and TRMM 3B42 show significant differences in precipitation distribution in the lighter to moderate rain categories in all the stations except

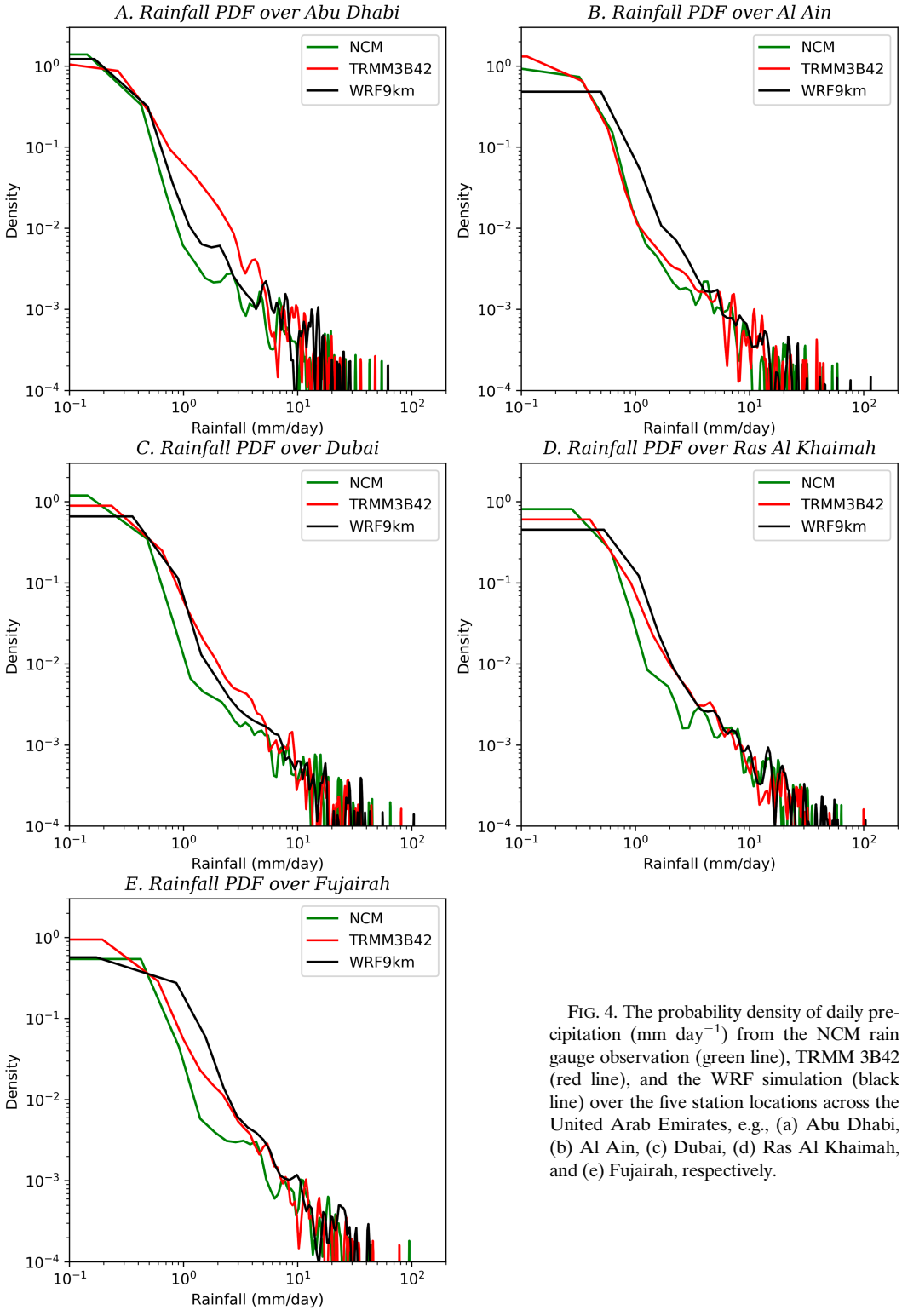

FIG. 4. The probability density of daily precipitation (mm day^{-1}) from the NCM rain gauge observation (green line), TRMM 3B42 (red line), and the WRF simulation (black line) over the five station locations across the United Arab Emirates, e.g., (a) Abu Dhabi, (b) Al Ain, (c) Dubai, (d) Ras Al Khaimah, and (e) Fujairah, respectively.

for Al Ain (Fig. 4b). Regardless, WRF exceeded the lighter and moderate rainfall (0.5–3 mm day^{-1}) at all station locations except Abu Dhabi (Fig. 4), leading to a higher annual mean precipitation in WRF compared to station data.

The winter season contributes almost 70% of the total annual precipitation over most regions north of 20°N (Figs. S3A–C), likely related to the activity of Mediterranean synoptic-scale systems (Kumar et al. 2015; de Vries et al. 2016, 2018; Patlakas

et al. 2019). Summer precipitation contribution is much weaker over the Middle Eastern area, and the precipitation band south of 20°N is mainly related to the seasonal modulation of the intertropical convergence zone (Figs. S3D–F). WRF simulation can capture these seasonal precipitation variations (Figs. S3C,F), and their large spatial contrasts, giving us further confidence in using the WRF simulation to investigate the mechanisms that drive the precipitation spatiotemporal variability.

Figures 5a and 5d compare the spatial distribution of winter season precipitation from TRMM 3B42 observation and 17 years of WRF simulation, both showing large meridional gradients and decreasing from the north toward the south. The winter season displays an apparent lower-level anticyclone over the Middle East (Fig. 5b), corresponding to a high pressure system over the region and a strong upper-level jet centered around 28°N (Fig. 5c). Similar seasonal patterns in precipitation (Fig. 5d) and circulation are seen in WRF simulation (Figs. 5e,f), demonstrating the skill of the WRF Model in representing major observed climatological characteristics.

b. *Role of the upper-level subtropical jet on the intraseasonal precipitation variations*

Due to the dominant contribution of winter precipitation (70% of annual rainfall) and the substantial differences in circulation patterns between winter and summer (figures not shown), we focus only on the winter as our representative season to understand the mechanism of precipitation variability. Since winter precipitation events are related to Mediterranean synoptic-scale systems, we first identify the passages of synoptic systems during winter over the AP in both the WRF simulation and observations (i.e., ERA5 and TRMM 3B42). From the 17 years of data, we identified 73 (68) winter season precipitation events in WRF (observations), with details given in methodology section 2c(1). In addition, we converted all the daily data into pentad data for facilitating our analysis of synoptic-scale processes. The pentad data identify the zeroth pentad when the precipitation band reaches the northern AP, including parts of the Arabian Gulf and surrounding northern United Arab Emirates (50°–55°E and 24°–26°N). Further, all the events are composited from two pentads earlier (i.e., pentad −2) to one pentad later (i.e., pentad +1), and all the large-scale thermodynamical and dynamical parameters are diagnosed to understand the precipitation mechanism.

The composited pentads (two pentads earlier to one pentad later) of the anomalous (with respect to the 17-yr climatology) rainfall, upper-level (400–100 hPa) wind, midlevel (700–400 hPa) vorticity, 850-hPa geopotential height, column-integrated precipitable water, and lower-level (surface–850 hPa) moist static energy are shown in Fig. 6, respectively. Precipitation first appears over the northwest corner of the domain (i.e., the Mediterranean region) two pentads earlier [Fig. 6a(1)] and subsequently propagates eastward and merges with another branch of precipitation from the Red Sea and the Arabian Sea by the zeroth pentad [Fig. 6a(2)]. The time evolution of the rain pattern confirms that it is highly related to the propagation of the Mediterranean weather system and its interactions with the tropical air mass from the Red Sea and the Arabian Sea.

To understand this precipitation mechanism, the upper-level atmospheric dynamics is examined. The upper-level jet is observed to strengthen in the northern part of the domain two pentads earlier [pentad −2; Fig. 6b(1)] and then intensify further and moved southward one pentad earlier [pentad −1; Fig. 6b(2)], ultimately resulting in a stronger organized jet that reaches the AP at pentad zero [Fig. 6b(3)]. One pentad later (pentad +1), the jet weakens and moves northward away from the AP Fig. 6b(4)]. Associated with the upper-level jet, midlevel positive vorticity is also seen over the northwest sector of the jet (Fig. 6c) in all of the four pentads. This midlevel positive vorticity creates a lower-level convergence via the Ekman pumping to its south. This lower-level convergence is reflected as a lower-level negative geopotential height anomaly at one pentad earlier over the AP [Fig. 6d(2)]. This convergence is also in phase with the existing low-level system upstream to the northwest corner one pentad earlier [Fig. 6d(2)]. The lower-level convergence further strengthens the low pressure systems and pushes the persistent anticyclones eastward at pentad zero [Fig. 6d(3)]. This low pressure further helps southwesterly winds converge warm, moist air over the AP, channeling it toward the Zagros Mountains. Convergence between the warm–moist air from the tropical region and cold–dry air from the Mediterranean region occurs at one pentad earlier (pentad −1). Subsequently, it reaches over the AP at pentad zero and moves further eastward in later pentads (Fig. 6d). Associated with this lower-level convergence, we also find moisture (Fig. 6e) and instability (Fig. 6f) over the AP at one pentad earlier (pentad −1) and moved eastward subsequently.

Similar patterns in precipitation, dynamical, and thermodynamical features are also observed from the TRMM 3B42 and ERA5 reanalysis data (Fig. S4), further confirming the good performance and the value of the WRF simulation for studying the precipitation behaviors and their connections to the dynamical and thermodynamical processes. To quantify the variations of the Arabian precipitation and its connections to the upper-level jets, we first define and compute the upper-level jet-related parameters (i.e., jet magnitude, location, width, and southern extensions) in the pentad data for all 17 winter seasons (i.e., November–April). The computation of the jet parameters is explained in section 2c(2) and similar methodology is applied to both the WRF simulation and ERA5 data.

We further analyze the interrelationship between the different jet parameters for the WRF and ERA5 data (Fig. 7). We found a strong correlation between jet magnitude and jet width (CC = 0.93), which suggests that a stronger jet is typically broader (Fig. 7a). The jet width and jet southern extension (Fig. 7b) are also well correlated (CC = −0.92). Similarly, jet magnitude and jet southern extension (Fig. 7c) are highly anticorrelated with each other as well (CC = −0.86). Taken together, stronger and broader jets extend further south (Fig. 7). This supports the hypothesis that when a stronger jet moves over the AP, it covers the southern Arabian regions. We need to understand quantitatively how the jet magnitudes and their

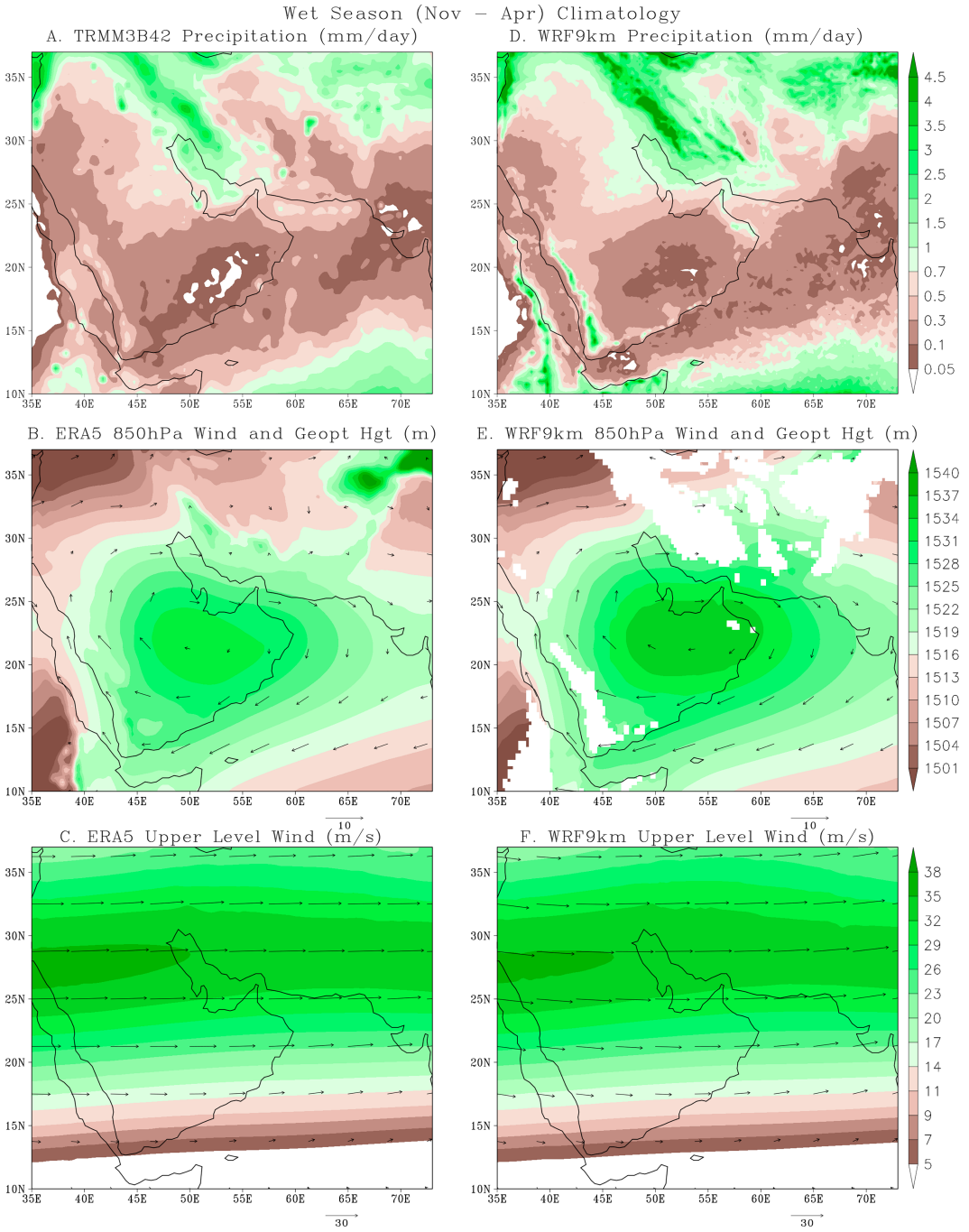

FIG. 5. The winter season (November–April) averaged (a) TRMM 3B42 precipitation (mm day^{-1}), (b) ERA5 850-hPa geopotential heights (m) along with circulation (m s^{-1}; vector), and (c) ERA5 upper-level (200 hPa) wind speed (m s^{-1}; shaded) and direction (vector). (d)–(f) As in (a)–(c), but for the WRF simulation.

southward expansion are associated with Arabian precipitation and its possible mechanism.

Table 1 shows the temporal correlation of different jet-related parameters with other parameters related to the Arabian precipitation for all 17 winter seasons, based on pentad data from the WRF simulation and observations (ERA5 and TRMM; within parentheses). The jet core magnitude in ERA5 has a stronger correlation with the temperature gradient and moist static energy (MSE) gradient, but it exhibits a weaker correlation (not significant at 99% confidence level based on the Student's *t* test) with midlevel vorticity followed by lower-level geopotential height and ultimately with AP precipitation. In contrast, the position of the jet's southern edge demonstrates a consistently stronger correlation (significant at the 99% confidence

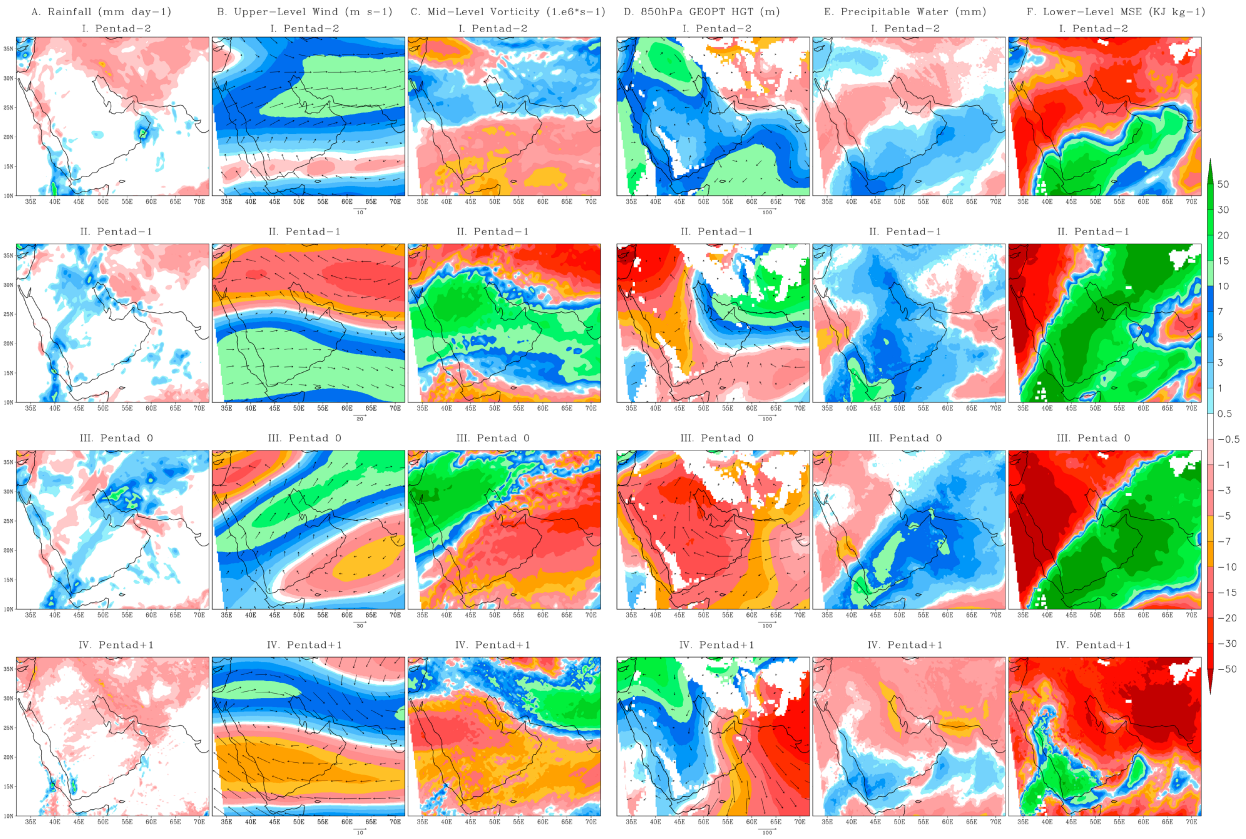

FIG. 6. (first row) The winter season (November–April) averaged anomalous (a) precipitation (mm day $^{-1}$), (b) upper-level (400–100 hPa) wind (m s^{-1}), (c) midlevel vorticity (s^{-1}), (d) lower-level (850 hPa) geopotential heights (m; shaded) with moisture flux vector (g m^{-2} s^{-1}), (e) column-integrated PW (mm), and (f) lower-level MSE (K J kg^{-1}) from the WRF simulation at two pentads earlier (pentad −2), respectively. (second row)–(fourth row) As in the first row, but for the pentad −1, pentad 0, and pentad +1 periods, respectively. The anomaly is calculated with respect to the 17-yr climatology conditions for all variables.

level based on the Student's *t* test) with all the variables, including precipitation over the AP. The results are consistent for the WRF simulation as well, which suggests that rainfall over the AP is significantly affected by the southward shift of the upper-level jet.

The above result conclusively demonstrates that a stronger upper-level jet and an upper-level trough are primarily associated with winter precipitation over the AP region. The southward shift of the upper-level jet induces midlevel vorticity over the Arabian and the Middle East regions. This vorticity further generates an anomalous lower-level convergence through Ekman pumping. This leads to the development of an anomalous surface low, which is further enhanced in the presence of the existing Red Sea trough over the AP. The surface low weakens the persistent lower-level anticyclone and causes it to shift eastward. The eastward displacement of the anticyclones allows the warm and moist air to enter the AP from the Arabian and the Red Seas. This warm and moist air converges with the cold and dry air from the midlatitude, promoting convection under favorable environmental conditions.

The pentad lead–lag composites of precipitation over the AP and their relationship with different parameters in Fig. 7d help to understand the direction of causality between our proposed mechanism and the Arabian precipitation. Here, the zero pentad is when precipitation happens over the AP. A stronger jet appears over the region at least two pentads earlier, peaks around one pentad earlier, and then starts weakening. However, the jet is not only stronger in two pentads earlier but also shifted southward. Its southern extent reaches around 16.5°N latitude at least one pentad earlier and remains there at pentad 0 when the precipitation peaks. As the precipitation starts to weaken one pentad later, the latitude of the jet's southern edge also retreats northward. So, a stronger jet is associated with positive midlevel vorticity (or cyclonic circulations), leading to the weakening of westerlies to the north and the strengthening of westerlies to the south, resulting in a southward shift of the jet. The southward shift of the jet further helps to bring moisture convergence and precipitation over the AP region. The results from the lead–lag map are very much consistent with our mechanism.

c. *Untangling jet-rainfall causal links via numerical experiments*

In this section, we demonstrate the direction of causality between the position of the upper-level jet and the AP precipitation using semi-idealized numerical experiments. WRF experiments to establish the causality between the upper-level jet and precipitation over the AP region are summarized in Table 2.

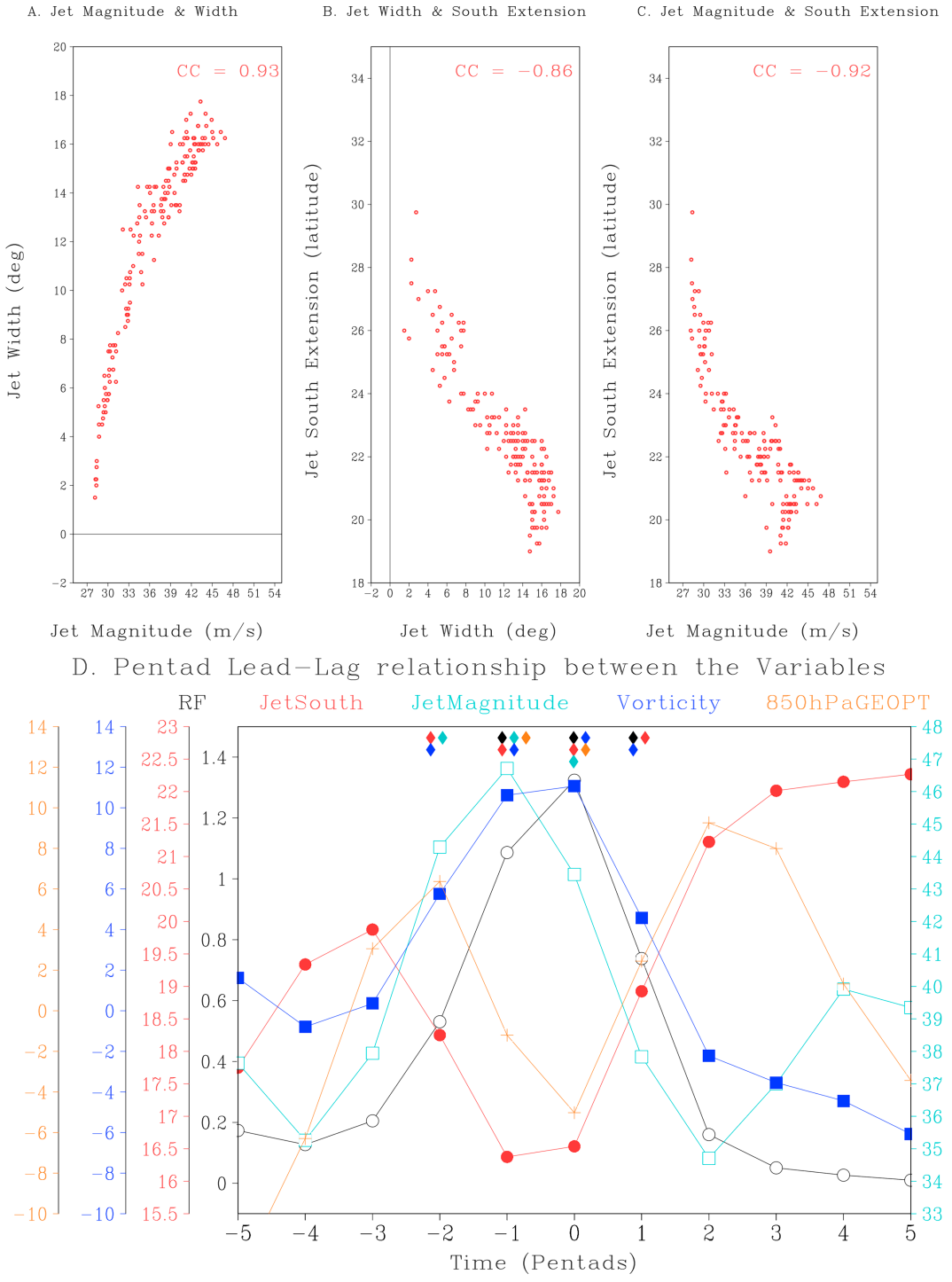

FIG. 7. The scatterplots of (a) jet core magnitude (m s^{-1}) vs jet width (°), (b) jet width (°) vs jet southern extension (lat), and (c) jet core magnitude (m s^{-1}) vs jet southern extension (lat), respectively. (d) The composited time evolution (in pentads) of precipitation (black line) over the Arabian Gulf and surrounding United Arab Emirates (50°–55°E and 24°–26°N), jet south locations (red; averaged over 40°–60°E), jet magnitudes (light blue; averaged over the region 1), midlevel (700–400 hPa) vorticity (blue; averaged over the region 1), and 850-hPa geopotential heights (orange; averaged over the region 1), respectively. The time evolutions are shown from five pentads earlier to five pentads later for all 73 events using WRF to understand the background conditions for AP precipitation. The solid diamonds in the upper portion of the figure in each pentad show significance at a 95% confidence level by the Student's *t* test.

TABLE 1. The time correlation of different jet-related parameters and physical parameters associated with Arabian precipitation for the winter season of all 17 years in the WRF simulation and observations (ERA5 and TRMM 3B42; within parentheses) using pentad data, respectively. Correlation values that are significant at the 99% confidence level as determined by the Student's *t* test are highlighted in bold.

Pentad values for 17 years WRF (ERA5 and TRMM)	Temperature gradient	MSE gradient	Midlevel vorticity	PW gradient	850-hPa geopotential height over AP	Precipitation over AP
Jet core magnitude	**0.83 (0.91)**	**0.57 (0.62)**	0.08 (−0.007)	**0.24 (0.22)**	−0.21 (−0.11)	−0.13 (−0.16)
Jet width	**0.68 (0.57)**	**0.42 (0.50)**	**0.50 (0.45)**	**0.35 (0.34)**	**−0.29** (−0.16)	0.13 (0.18)
Jet south location	**−0.51 (−0.36)**	**−0.32 (−0.36)**	**−0.59 (−0.60)**	**−0.35 (−0.32)**	**0.26 (0.19)**	**−0.22 (−0.23)**
850-hPa geopotential height over AP	**−0.30 (−0.31)**	**−0.29 (−0.21)**	**−0.21 (−0.42)**	**−0.23** (−0.14)	—	**−0.25 (−0.26)**
Precipitation over AP	0.003 (−0.10)	**0.35 (0.32)**	**0.44 (0.36)**	**0.56 (0.52)**	**−0.25 (−0.26)**	—

As case studies, we chose a heavy precipitation event associated with the strong upper-level jet (Fig. 8a) from 11 to 27 January 2009 (named "Jan2009-Control") and a rain-free case in the presence of a climatological jet (Fig. 8d) over the AP (6–22 March 2009; "Mar2009-Control") to test our hypothesis. The control simulation of the January event (Jan2009-Control) shows the presence of precipitation over the Iranian plateau and its southward extension over the AP (Fig. 8b). We performed another numerical experiment, called Jan2009-Experiment, by replacing only the upper-level (400–100 hPa) zonal (u) and meridional (v) wind in the Jan2009-Control case with the Mar2009-Control case (there is a weaker jet with no southward extension) in the lateral boundaries of the WRF simulation domain while keeping all the other three-dimensional variables (e.g., temperature, moisture, geopotential) and surface variables (U10, V10, surface pressure, etc.) as well as all the initial conditions the same as the Jan2009-Control conditions. At the same time, spectral nudging is used for the first 3 days to relax the horizontal wind with a meridional wavenumber of 0–2 and zonal wavenumber of 0–4 to constrain the large-scale flow and convergence in the domain and allow for the mesoscale to saturate in the spectral space (Zhang et al. 2017; Taraphdar et al. 2021).

Consistent with our hypothesis, "Jan2009-Experiment" shows a significant reduction in precipitation over the AP (Fig. 8c), and most of the precipitation occurs north of the 30°N latitude. We also performed a counter experiment, called "Mar2009-Experiment," by replacing the Mar2009-Control wind (Fig. 8d) with the Jan2009-Control wind (Fig. 8a) but keeping all the other three-dimensional and surface variables as in the Mar2009-Control conditions. The Mar2009-Control shows almost no precipitation over the AP (south of 25°N; Fig. 8e), but a substantial increase in precipitation over the AP is found in Mar2009-Experiment (Fig. 8f) just by placing the upper-level jet over the AP. These experiments are conclusive enough to show that a strong and southward-extended jet can indeed produce rainfall over the AP. Our results reflect the conjecture that a stronger jet is necessary for winter precipitation over the AP, and its southward extension is vital.

d. *Can the upper-level jet explain the interannual precipitation variability?*

To check the robustness of our hypothesis, we further test it by analyzing dry and wet years to see if it can explain the interannual precipitation variability. The procedure to identify wet and dry years is described in section 2c(3). The interannual

TABLE 2. Description of different numerical experiments to demonstrate the direction of causality between the position of upper-level jet and Arabian precipitation.

Experiment	Description	Method
Jan2009-Control	Control simulation for the heavy precipitation event associated with a strong, southward-shifted upper-level (400–100 hPa) jet during 11–27 Jan 2009	WRF simulation using initial and boundary conditions from ERA5 corresponding to the heavy precipitation event days (11–27 Jan 2009)
Mar2009-Control	Control simulation for a rain-free event in the presence of a climatological upper-level jet during 6–22 Mar 2009	WRF simulation using initial and boundary conditions from ERA5 corresponding to the rain-free event days (6–22 Mar 2009)
Jan2009-Experiment	Experiment to demonstrate the reduction in rainfall when a strong upper-level jet is replaced with a climatological jet	Replace the upper-level zonal (u) and meridional (v) wind of the heavy precipitation event by the rain-free event in WRF lateral boundary conditions but keeping all other variables as well as initial conditions the same as Jan2009-Control
March2009-Experiment	Experiment to demonstrate the increase in rainfall in the presence of a stronger, southward-shifted upper-level jet	Similar to Jan2009-Experiment, but the climatological upper-level jet is replaced by the strong upper-level jet

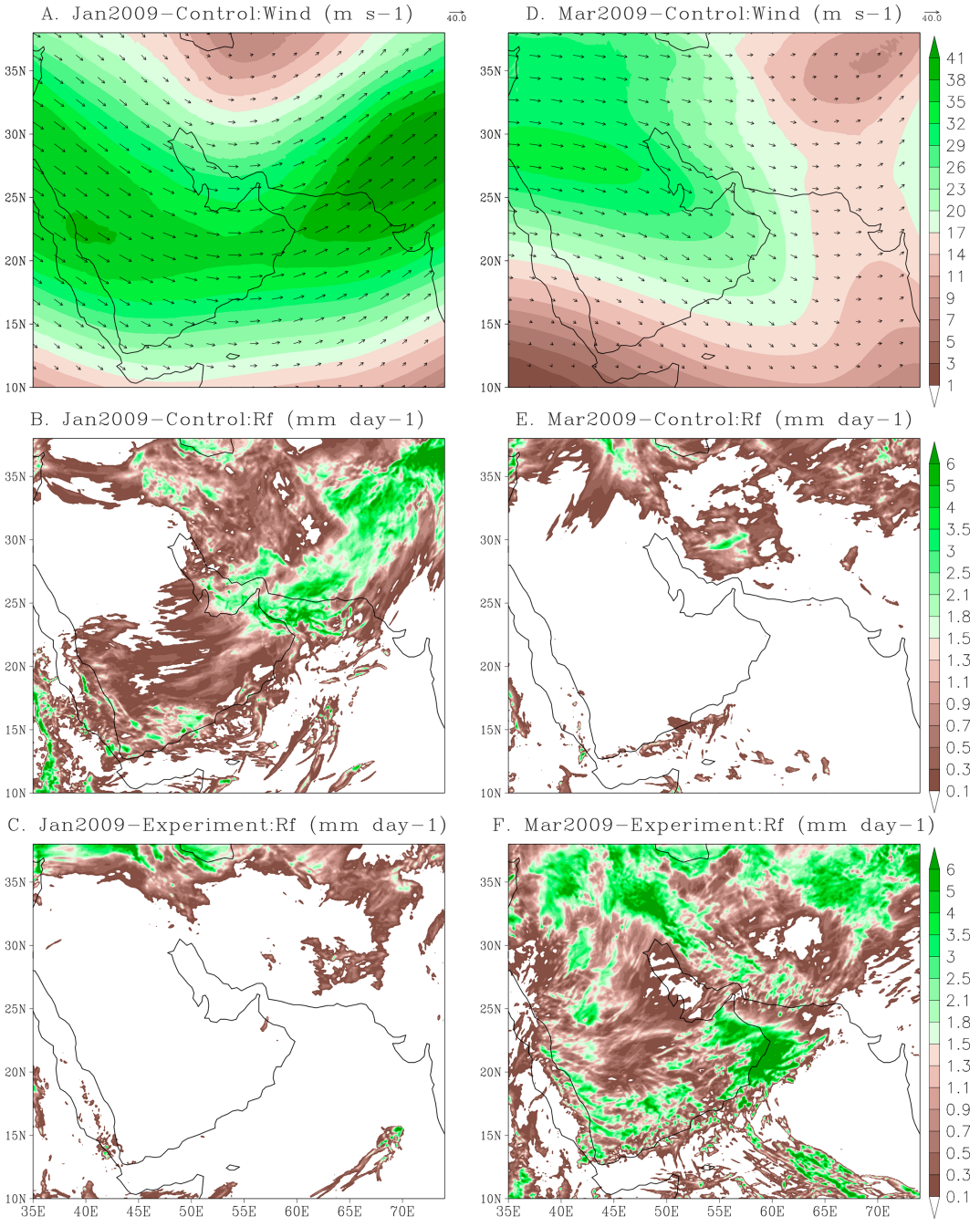

FIG. 8. (a),(d) The upper-level (400–100 hPa averaged) wind speed (shaded; m s^{-1}) and circulation (wind vector) during a strong precipitation event (11–27 Jan 2009; Jan2009-Control) and an episode without precipitation (6–22 Mar 2009; Mar2009-Control) over the AP, respectively. (b),(e) The model precipitation (mm day^{-1}) from the Jan 2009-Control and Mar 2009-Control, respectively. (c) As in (b), but for the experiment when the upper-level (400–100 hPa) zonal (u) and meridional (v) wind are replaced in the Jan2009-Control case by the Mar2009-Control case. (f) As in (c), but for the Mar2009-Experiment.

precipitation evolution and its climatological mean over the AP in WRF, TRMM 3B42, and CHIRPS are consistent (Fig. S5A). Precipitation in the WRF simulation and two observational datasets is strongly correlated, which documents that stronger and weaker precipitation years are similar in the observation and the WRF simulation. Three wet years (2005, 2006, and 2016) and three dry years (2008, 2010, and 2015) are identified from the 17-yr dataset (Fig. S5B). We composite them to explore if our mechanism can explain the differences in precipitation between wet and dry years.

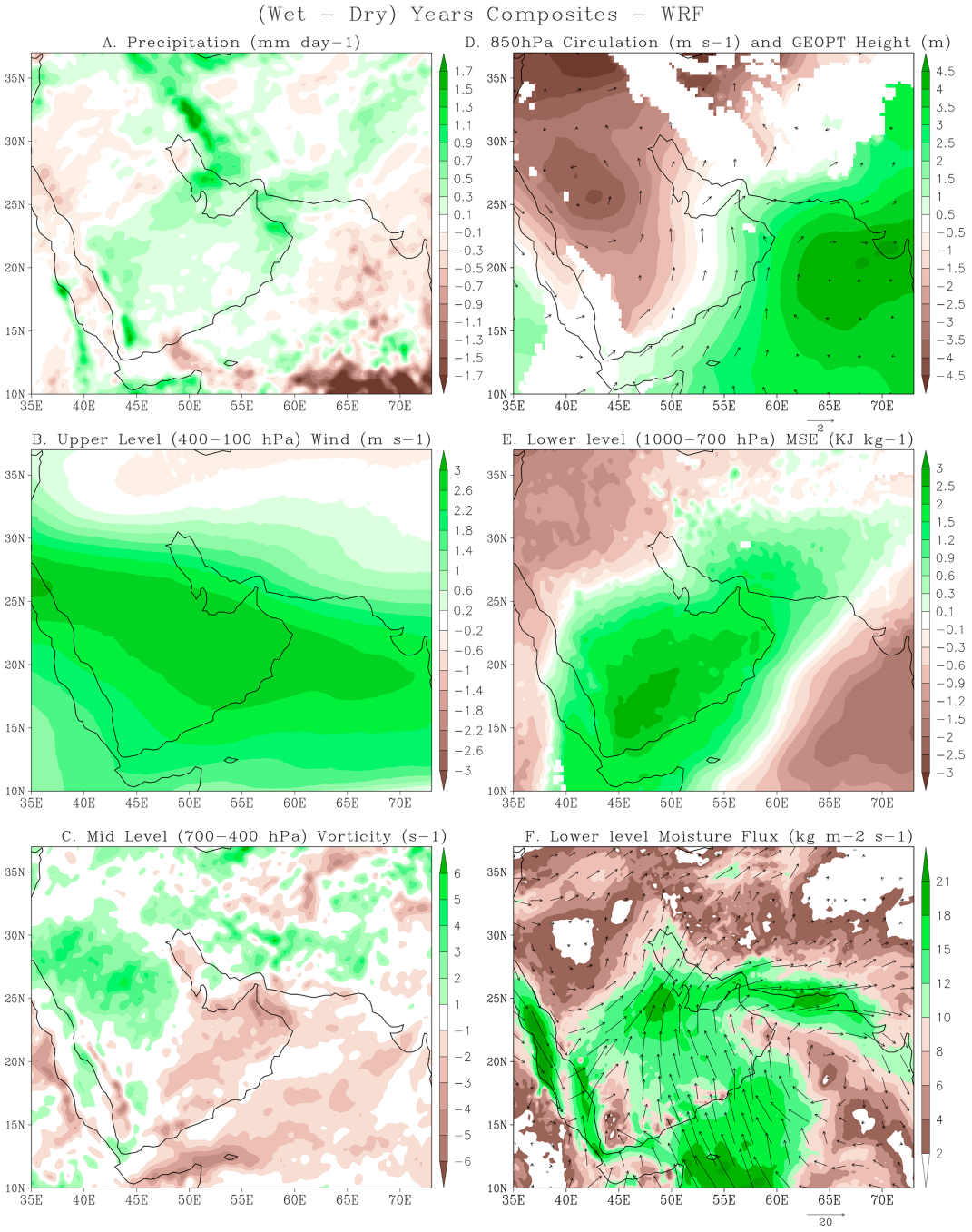

FIG. 9. The difference between the "wet" and "dry" year composites: (a) precipitation (mm day^{-1}), (b) upper-level (400–100 hPa) wind speed (m s^{-1}), (c) midlevel (700–400 hPa) vorticity (s^{-1}), (d) 850-hPa circulation (vector) and geopotential height (m; shaded), (e) lower-level (1000–700 hPa) MSE (kJ kg^{-1}), and (f) lower-level moisture flux (kg m^{-2} s^{-1}) from the WRF simulation.

The composited difference in WRF precipitation between wet and dry years (Fig. 9a) shows that the rainfall difference is most prominent over the Zagros Mountains region, extending to the AP. The differences are less prominent south of 20° since the region is mostly dominated by summertime precipitation, other than some oceanic areas over the Arabian Sea. Substantial differences in rainfall north of 25°N indicate its possible connection with the midlatitude jet. The upper-level (400–100 hPa) jet is stronger during the wet years and shifts southward over the AP compared to the dry years (Fig. 9b). A stronger jet generates anomalous midlevel vorticity (Fig. 9c), further creating anomalous lower-level convergence (Fig. 9d).

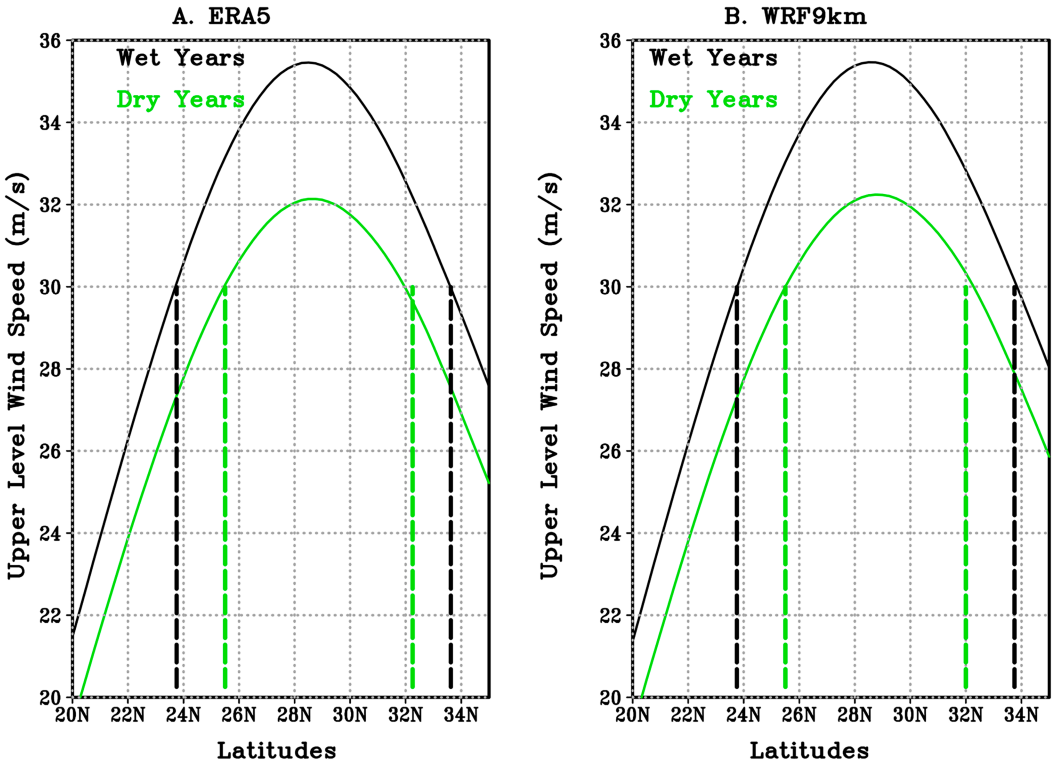

FIG. 10. The latitudinal distribution of upper-level (400–100 hPa) wind magnitude (m s^{-1}) averaged over the longitudes (40°–60°E) during wet years (black curve) and dry years (green curve) in both (a) ERA5 and (b) the WRF simulation, respectively.

The eastward shift of the anticyclone (Fig. 9d) helps to generate moisture convergence over the Arabian Gulf and subsequently the AP. Consistent with this moisture convergence, the AP also features more substantial lower-level instability (Fig. 9e), more column-integrated precipitable water (PW; figure not shown), and stronger moisture transport from the Arabian Sea and Red Sea (Fig. 9f). These processes create favorable conditions for precipitation and help to generate more rainfall in wet years compared to dry years. Our mechanism is also supported by the observation-based diagnosis using TRMM 3B42 precipitation and ERA5 reanalysis (Fig. S6).

We have further extended our analysis period to encompass 43 years, from 1981 to 2023 based on the ERA5 reanalysis data and identified six wet years (1982, 1988, 1991, 1994, 1996, 2010) and seven dry years (1993, 1999, 2000, 2007, 2009, 2021, 2022), respectively. We composited the data from these years and found very similar results, like an increase in precipitation over the AP during wet years compared to dry years, consistent with an increase in the upper-level jet strength in the southern region followed by an increase in midlevel positive vorticity over the AP (figure not shown). These all suggest that our results are consistent even if we change the time period and increase the samples of wet and dry years.

Since the strength and location of the jet qualitatively explain the difference in precipitation between wet and dry years, we quantify the changes in jet magnitude and its location. Figure 10 displays the latitude distribution of upper-level (400–100 hPa) wind magnitude averaged over the longitude 40°–60°E during wet and dry years in both ERA5 (Fig. 10a) and WRF simulation (Fig. 10b). Figure 10 demonstrates that during wet years (35.5 m s^{-1}), the jet peak magnitude is about 3 m s^{-1} stronger compared to dry years (32.2 m s^{-1}) and is also wider by about 3°. Specifically, the jet extends southward (or equatorward) by about 2° latitude during wet years.

Now, we separate the impacts of jet magnitude and its southward extension in the abovementioned physical processes. The left panels of Fig. 11 show the scatterplot of different parameters related to precipitation (e.g., midlevel vorticity anomaly, lower-level geopotential height anomaly, vertically integrated PW anomaly, and AP precipitation anomaly) with the jet core magnitude anomaly with respect to the climatology (17 years) during wet (blue) and dry (red) years, respectively. Midlevel vorticity does not correlate with jet core magnitude (Fig. 11a) but is strongly correlated with the southern extension of the jet (Fig. 11e). The jet's southern extension can explain about 13.7% of vorticity variability during wet years compared to 2.6% during dry years. Wet years show a more pronounced southward jet extension than the jet core magnitude. But in the case of lower-level geopotential heights, both the jet core magnitude and its southward extension contribute comparably (Figs. 11b,f). For PW anomaly, the jet's southern extension is more strongly correlated with the PW anomaly than the jet core magnitude, specifically during wet years (Figs. 11c,g). In the wet years, the jet core magnitude (19.4%) explains a much smaller PW anomaly than

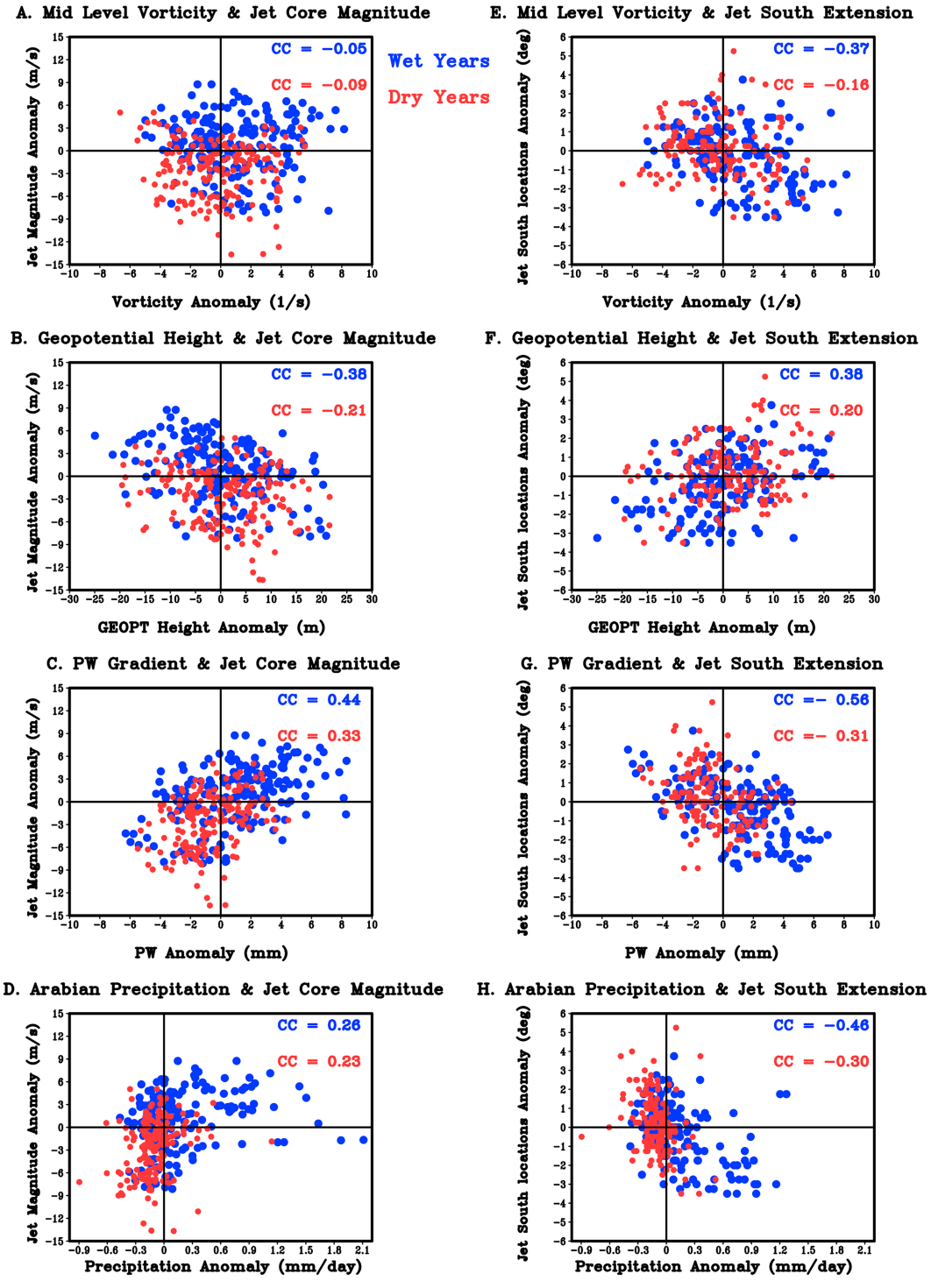

FIG. 11. The scatter diagram of (a) midlevel vorticity anomaly (s^{-1}), (b) lower-level geopotential height anomaly (m), (c) vertically integrated PW anomaly (mm), and (d) AP precipitation anomaly (mm day^{-1}) with the jet core magnitude anomaly (m s^{-1}) with respect to the 17-yr climatology during wet (blue) and dry (red) years, respectively. (e)–(h) As in (a)–(d), but for the jet southern location anomaly (degrees lat), respectively. Each dot in every panel represents the single pentad values.

the jet's southern extension (31.4%). Identical to the PW anomaly, precipitation over the AP correlates better with the southward jet extension, specifically during wet years (Figs. 11d,h). The southward jet extension can explain (21.2%) almost 3 times more precipitation variability than the jet magnitude (6.8%) during wet years. This suggests that a southward shift of the jet might be more critical for the AP precipitation compared to the jet core magnitude.

4. Summary and conclusions

A 17-yr (2002–18) long simulation was performed using the WRF Model at a gray-zone resolution to understand the climatological, intraseasonal, and interannual variability of precipitation over the AP. The WRF simulation at a 9-km grid length without the convective parameterization can capture the precipitation climatology and interannual variabilities well. We find that winter precipitation contributes almost 70% of annual rainfall over the AP and the United Arab Emirates and is mainly associated with the movement of the Mediterranean synoptic-scale systems. Winter season precipitation first appears over the northwest corner of the domain (i.e., Mediterranean region) two pentads earlier. It then propagates eastward and merges with another branch of precipitation from the Red Sea and the Arabian Sea by the zeroth pentad. This time evolution of the rain pattern confirms that winter season precipitation is mainly related to the propagation of the Mediterranean systems and their interactions with the tropical air mass from the Red Sea and the Arabian Sea.

Consistent with the precipitation, the circulation also indicates an organization of the upper-level jet two pentads earlier over the Middle East, which establishes a stronger jet over the AP one pentad earlier. This stronger upper-level jet over the AP creates midlevel vorticity and lower-level convergence one pentad earlier, which weakens the persistent anticyclones and displaces them eastward. This process strengthens the moisture convergence and instability in the lower level, allowing precipitation initiation at the zeroth pentad over the AP. Figure 12 illustrates the precipitation mechanism proposed in this study, which is outlined as follows. Winter season precipitation events over the AP are primarily associated with a stronger and broader upper-level jet. The southward shift of the upper-level jet induces positive midlevel vorticity (shaded yellow in Fig. 12) over the AP and the associated Middle East region. This positive vorticity creates a lower-level convergence zone (CZ) through Ekman pumping over the AP. This leads to the development of an anomalous surface low, which is then enhanced in the presence of the existing Red Sea trough. This surface low weakens the persistent anticyclone [lower-level anticyclone (LAC)] over the AP and shifts it eastward to the Arabian Sea. The eastward shift of the lower-level anticyclone allows the warm and moist air from the Arabian and the Red Seas to enter the AP. This warm and moist air converges with the cold and dry air from the midlatitude and initiates the convection under favorable environmental conditions.

We tested this hypothesis by examining the precipitation differences between the wet and dry years. WRF can realistically capture the precipitation difference between the wet and dry years and its association with upper-level jets. A roughly 2° southward shift of the upper-level jet along with about a 3 m s^{-1} stronger jet peak magnitude helps to build the warmer midlevel and lower-level instability, leading to stronger precipitation over the Arabian Gulf regions during wet years. The current research identifies that the more substantial precipitation during wet years is primarily associated with a stronger and broader upper-level jet than in dry years. The southward shift of the jet can explain about 21% of the AP's precipitation variability compared to the 7% demonstrated by the jet core magnitude during wet years, suggesting the importance of the jet's southward shift for wet years over the AP.

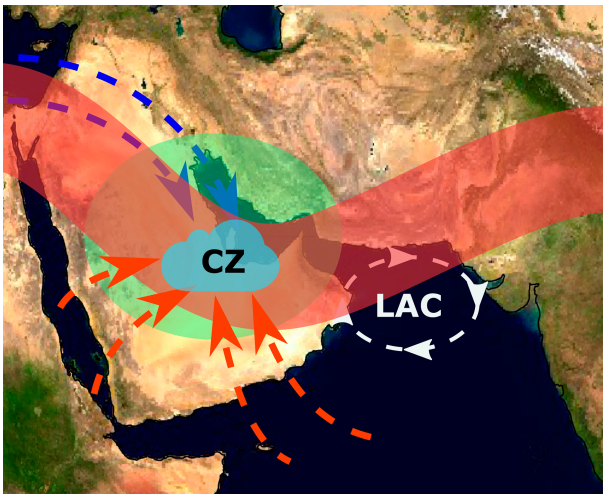

FIG. 12. A schematic representation of our mechanism. The upper-level jet is the red shaded area, green shaded area is the midlevel vorticity, and lower-level convergence (CZ) is in blue shading. The blue color dashed arrow signifies the cold dry air, and the red dashed arrow shows as the warm moist air, respectively.

The current study provides guidance for robust regional climate simulations over the AP and the mechanism behind the winter season precipitation. We plan to investigate shift of the upper-level jet under future climate warming scenarios and their impact on future precipitation over the AP region.

Acknowledgments. This work is supported by the National Center of Meteorology (NCM), Abu Dhabi, United Arab Emirates, under the UAE Research Program for Rain Enhancement Science. The NCM is greatly acknowledged for providing the rain-gauge data over the United Arab Emirates under an agreement with clauses for nondisclosure of data. The authors acknowledge the 3-hourly precipitation data from the TRMM 3B42 and CHIRPS. We also acknowledge the National Center for Atmospheric Research (NCAR) for developing and supporting the WRF Model and the ECMWF for providing the ERA5 data. The lead author was funded by the Arabian Center for Climate and Environmental Sciences (ACCESS), New York University Abu Dhabi (NYUAD), through the Research Institute Grant. The lead author, L. Ruby Leung and Samson Hagos were also supported by the Office of Sciences, U.S. Department of Energy (DOE)

Biological and Environmental Research, as part of the Water Cycle and Climate Extremes Modeling (WACCEM) Scientific Focus Area funded by the Regional and Global Model Analysis program area. Pacific Northwest National Laboratory is operated for DOE by Battelle Memorial Institute under contract DE-AC05-76RL01830. The authors acknowledge the JUBAIL/DALMA high-performance computing resources at NYUAD for the WRF Model simulation as well as the analyses of the data that have contributed to the research results reported in this paper.

Data availability statement. The 3-hourly TRMM 3B42 precipitation data can be accessed from NASA at https://disc.gsfc.nasa.gov/datasets?keywords=TMPA&page=1, and the CHIRPS precipitation data can be accessed from https://data.chc.ucsb.edu/products/CHIRPS-2.0/. The ERA5 datasets are available from ECMWF at https://cds.climate.copernicus.eu/datasets/reanalysis-era5-pressure-levels?tab=download. The access for NCM rain-gauge station data is restricted and readers should send their request to NCM. WRF Model output is stored and can be accessed through the JUBAIL/DALMA data archive policy.

REFERENCES

Alizadeh, Z., A. R. Mohebalhojeh, F. Ahmadi-Givi, M. Mirzaei, and S. Khansalari, 2021: The climatological impact of the upper-tropospheric Rossby wave propagation on the Red Sea trough in winter. *Atmos. Res.*, **250**, 105368, https://doi.org/10.1016/j.atmosres.2020.105368.

Almazroui, M., 2011: Sensitivity of a regional climate model on the simulation of high intensity rainfall events over the Arabian Peninsula and around Jeddah (Saudi Arabia). *Theor. Appl. Climatol.*, **104**, 261–276, https://doi.org/10.1007/s00704-010-0387-3.

——, 2012: Dynamical downscaling of rainfall and temperature over the Arabian Peninsula using RegCM4. *Climate Res.*, **52**, 49–62, https://doi.org/10.3354/cr01073.

——, 2016: RegCM4 in climate simulation over CORDEX-MENA/Arab domain: Selection of suitable domain, convection and land-surface schemes. *Int. J. Climatol.*, **36**, 236–251, https://doi.org/10.1002/joc.4340.

——, M. Nazrul Islam, H. Athar, P. D. Jones, and M. A. Rahman, 2012: Recent climate change in the Arabian Peninsula: Annual rainfall and temperature analysis of Saudi Arabia for 1978–2009. *Int. J. Climatol.*, **32**, 953–966, https://doi.org/10.1002/joc.3446.

Al-Nassar, A. R., J. L. Pelegrí, P. Sangrà, M. Alarcon, and A. Jansa, 2020: Cut-off low systems over Iraq: Contribution to annual precipitation and synoptic analysis of extreme events. *Int. J. Climatol.*, **40**, 908–926, https://doi.org/10.1002/joc.6247.

Alsubhi, Y. H., A. M. Awad, A.-W. S. Mashat, and A. H. Labban, 2023: Climatology of the spring subtropical jet stream over the Middle East and its effect on the synoptic characteristics of dust systems over the northern Arabian Peninsula. *Arabian J. Geosci.*, **16**, 669, https://doi.org/10.1007/s12517-023-11788-1.

Armon, M., F. Marra, Y. Enzel, D. Rostkier-Edelstein, and E. Morin, 2020: Radar-based characterisation of heavy precipitation in the eastern Mediterranean and its representation in a convection-permitting model. *Hydrol. Earth Syst. Sci.*, **24**, 1227–1249, https://doi.org/10.5194/hess-24-1227-2020.

Atif, R. M., M. Almazroui, S. Saeed, M. A. Abid, M. N. Islam, and M. Ismail, 2020: Extreme precipitation events over Saudi Arabia during the wet season and their associated teleconnections. *Atmos. Res.*, **231**, 104655, https://doi.org/10.1016/j.atmosres.2019.104655.

Attada, R., and Coauthors, 2020: Evaluating cumulus parameterization schemes for the simulation of Arabian Peninsula winter rainfall. *J. Hydrometeor.*, **21**, 1089–1114, https://doi.org/10.1175/JHM-D-19-0114.1.

——, H. P. Dasari, R. Ghostine, N. K. Kondapalli, R. K. Kunchala, T. M. Luong, and I. Hoteit, 2022: Diagnostic evaluation of extreme winter rainfall events over the Arabian Peninsula using high-resolution weather research and forecasting simulations. *Meteor. Appl.*, **29**, e2095, https://doi.org/10.1002/met.2095.

Chen, X., O. M. Pauluis, and F. Zhang, 2018: Regional simulation of Indian summer monsoon intraseasonal oscillations at gray-zone resolution. *Atmos. Chem. Phys.*, **18**, 1003–1022, https://doi.org/10.5194/acp-18-1003-2018.

de Vries, A. J., E. Tyrlis, D. Edry, S. O. Krichak, B. Steil, and J. Lelieveld, 2013: Extreme precipitation events in the Middle East: Dynamics of the Active Red Sea Trough. *J. Geophys. Res. Atmos.*, **118**, 7087–7108, https://doi.org/10.1002/jgrd.50569.

——, S. B. Feldstein, M. Riemer, E. Tyrlis, M. Sprenger, M. Baumgart, M. Fnais, and J. Lelieveld, 2016: Dynamics of tropical–extratropical interactions and extreme precipitation events in Saudi Arabia in autumn, winter and spring. *Quart. J. Roy. Meteor. Soc.*, **142**, 1862–1880, https://doi.org/10.1002/qj.2781.

——, H. G. Ouwersloot, S. B. Feldstein, M. Riemer, A. M. El Kenawy, M. F. McCabe, and J. Lelieveld, 2018: Identification of tropical-extratropical interactions and extreme precipitation events in the Middle East based on potential vorticity and moisture transport. *J. Geophys. Res. Atmos.*, **123**, 861–881, https://doi.org/10.1002/2017JD027587.

Evans, J. P., R. B. Smith, and R. J. Oglesby, 2004: Middle East climate simulation and dominant precipitation processes. *Int. J. Climatol.*, **24**, 1671–1694, https://doi.org/10.1002/joc.1084.

Fonseca, R., and Coauthors, 2020: On the analysis of the performance of WRF and NICAM in a hyperarid environment. *Wea. Forecasting*, **35**, 891–919, https://doi.org/10.1175/WAF-D-19-0210.1.

Francis, D., M. Temimi, R. Fonseca, N. R. Nelli, R. Abida, M. Weston, and Y. Whebe, 2021: On the analysis of a summertime convective event in a hyperarid environment. *Quart. J. Roy. Meteor. Soc.*, **147**, 501–525, https://doi.org/10.1002/qj.3930.

Funk, C., and Coauthors, 2015: The climate hazards infrared precipitation with stations—A new environmental record for monitoring extremes. *Sci. Data*, **2**, 150066, https://doi.org/10.1038/sdata.2015.66.

Gopalakrishnan, D., and Coauthors, 2023: Anatomy of a summertime convective event over the Arabian region. *Mon. Wea. Rev.*, **151**, 989–1004, https://doi.org/10.1175/MWR-D-22-0082.1.

Held, I. M., 1975: Momentum transport by quasi-geostrophic eddies. *J. Atmos. Sci.*, **32**, 1494–1497, https://doi.org/10.1175/1520-0469(1975)032<1494:MTBQGE>2.0.CO;2.

Hersbach, H., B. Bell, P. Berrisford, S. Hirahara, and A. Horányi, 2020: The ERA5 global reanalysis. *Quart. J. Roy. Meteor. Soc.*, **146**, 1999–2049, https://doi.org/10.1002/qj.3803.

Horan, M. F., F. Batibeniz, F. Kucharski, M. Almazroui, M. A. Abid, J. S. Fu, and M. Ashfaq, 2023: Moisture sources for precipitation variability over the Arabian Peninsula. *Climate Dyn.*, **61**, 4793–4807, https://doi.org/10.1007/s00382-023-06762-2.

Hussain, A., and M. Van Den Broeke, 2015: Using the WRF regional climate model to simulate future summertime wind speed changes over the Arabian Peninsula. *J. Climatol. Wea. Forecasting*, **3**, 1000144, https://doi.org/10.4172/2332-2594.1000144.

Iacono, M. J., J. S. Delamere, E. J. Mlawer, M. W. Shephard, S. A. Clough, and W. D. Collins, 2011: Radiative forcing by long-lived greenhouse gases: Calculations with the AER radiative transfer models. *J. Geophys. Res.*, **113**, D13103, https://doi.org/10.1029/2008JD009944.

Iguchi, T., T. Kozu, R. Meneghini, J. Awaka, and K. I. Okamoto, 2000: Rain-profiling algorithm for the TRMM precipitation radar. *J. Appl. Meteor.*, **39**, 2038–2052, https://doi.org/10.1175/1520-0450(2001)040<2038:RPAFTT>2.0.CO;2.

Jing, X., B. Geerts, Y. Wang, and C. Liu, 2017: Evaluating seasonal orographic precipitation in the interior western United States using gauge data, gridded precipitation estimates, and a regional climate simulation. *J. Hydrometeor.*, **18**, 2541–2558, https://doi.org/10.1175/JHM-D-17-0056.1.

——, and Coauthors, 2020: Convection-permitting regional climate simulations in the Arabian Gulf region using WRF driven by bias-corrected GCM data. *J. Climate*, **33**, 7787–7815, https://doi.org/10.1175/JCLI-D-20-0155.1.

Kumar, K. N., D. Entekhabi, and A. Molini, 2015: Hydrological extremes in hyperarid regions: A diagnostic characterization of intense precipitation over the central Arabian Peninsula. *J. Geophys. Res. Atmos.*, **120**, 1637–1650, https://doi.org/10.1002/2014JD022341.

——, T. B. M. J. Ouarda, S. Sandeep, and R. S. Ajayamohan, 2016: Wintertime precipitation variability over the Arabian Peninsula and its relationship with ENSO in the CAM4 simulations. *Climate Dyn.*, **47**, 2443–2454. , https://doi.org/10.1007/s00382-016-2973-2.

Li, C., and J. J. Wettstein, 2012: Thermally driven and eddy-driven jet variability in reanalysis. *J. Climate*, **25**, 1587–1596, https://doi.org/10.1175/JCLI-D-11-00145.1.

Liu, C., and Coauthors, 2017: Continental-scale convection-permitting modeling of the current and future climate of North America. *Climate Dyn.*, **49**, 71–95, https://doi.org/10.1007/s00382-016-3327-9.

Milewski, A., R. Elkadiri, and M. Durham, 2015: Assessment and comparison of TMPA satellite precipitation products in varying climatic and topographic regimes in Morocco. *Remote Sens.*, **7**, 5697–5717, https://doi.org/10.3390/rs70505697.

Nesbitt, S. W., and E. J. Zipser, 2003: The diurnal cycle of rainfall and convective intensity according to three years of TRMM measurements. *J. Climate*, **16**, 1456–1475, https://doi.org/10.1175/1520-0442(2003)016%3C1456:TDCORA%3E2.0.CO;2.

Niu, G.-Y., and Coauthors, 2011: The community Noah land surface model with multiparameterization options (Noah-MP): 1. Model description and evaluation with local-scale measurements. *J. Geophys. Res.*, **116**, D12109, https://doi.org/10.1029/2010JD015139.

Patlakas, P., C. Stathopoulos, H. Flocas, C. Kalogeri, and G. Kallos, 2019: Regional climatic features of the Arabian Peninsula. *Atmosphere*, **10**, 220, https://doi.org/10.3390/atmos10040220.

Pauluis, O., and S. Garner, 2006: Sensitivity of radiative–convective equilibrium simulations to horizontal resolution. *J. Atmos. Sci.*, **63**, 1910–1923, https://doi.org/10.1175/JAS3705.1.

Rasmussen, K. L., A. F. Prein, R. M. Rasmussen, K. Ikeda, and C. Liu, 2020: Changes in the convective population and thermodynamic environments in convection-permitting regional climate simulations over the United States. *Climate Dyn.*, **55**, 383–408, https://doi.org/10.1007/s00382-017-4000-7.

Ren, Q., W. Wei, M. Lu, and S. Yang, 2022: Dynamical analysis of the winter middle east jet stream and comparison with the East Asian and North American jet streams. *J. Climate*, **35**, 4455–4468, https://doi.org/10.1175/JCLI-D-21-0664.1.

Saeed, S., and M. Almazroui, 2019: Impacts of mid-latitude circulation on winter precipitation over the Arabian Peninsula. *Climate Dyn.*, **53**, 5253–5264, https://doi.org/10.1007/s00382-019-04862-6.

Sandeep, S., and R. S. Ajayamohan, 2018: Modulation of winter precipitation dynamics over the Arabian Gulf by ENSO. *J. Geophys. Res. Atmos.*, **123**, 198–210, https://doi.org/10.1002/2017JD027263.

Satoh, M., and Coauthors, 2014: The Non-hydrostatic Icosahedral Atmospheric Model: Description and development. *Prog. Earth Planet. Sci.*, **1**, 18, https://doi.org/10.1186/s40645-014-0018-1.

Schumacher, C., and R. A. Houze Jr., 2000: Comparison of radar data from the TRMM satellite and Kwajalein oceanic validation site. *J. Appl. Meteor.*, **39**, 2151–2164, https://doi.org/10.1175/1520-0450(2001)040<2151:CORDFT>2.0.CO;2.

Schwitalla, T., O. Branch, and V. Wulfmeyer, 2020: Sensitivity study of the planetary boundary layer and microphysical schemes to the initialization of convection over the Arabian Peninsula. *Quart. J. Roy. Meteor. Soc.*, **146**, 846–869, https://doi.org/10.1002/qj.3711.

Skamarock, W. C., and Coauthors, 2019: A description of the Advanced Research WRF Model version 4. NCAR Tech. Note NCAR/TN-556+STR, 145 pp., https://doi.org/10.5065/1dfh-6p97.

Sukoriansky, S., B. Galperin, and V. Perov, 2005: Application of a new spectral theory of stably stratified turbulence to the atmospheric boundary layer over sea ice. *Bound.-Layer Meteor.*, **117**, 231–257, https://doi.org/10.1007/s10546-004-6848-4.

Taraphdar, S., and O. M. Pauluis, 2021: Impact of planetary boundary layer and cloud microphysics on the sensitivity of monsoon precipitation using a gray-zone regional model. *Earth Space Sci.*, **8**, e2020EA001535, https://doi.org/10.1029/2020EA001535.

——, P. Mukhopadhyay, L. R. Leung, F. Zhang, S. Abhilash, and B. N. Goswami, 2014: The role of moist processes in the intrinsic predictability of Indian Ocean cyclones. *J. Geophys. Res. Atmos.*, **119**, 8032–8048, https://doi.org/10.1002/2013JD021265.

——, and Coauthors, 2021: WRF gray-zone simulations of precipitation over the Middle-East and the UAE: Impacts of physical parameterizations and resolution. *J. Geophys. Res. Atmos.*, **126**, e2021JD034648, https://doi.org/10.1029/2021JD034648.

Thompson, G., and T. Eidhammer, 2014: A study of aerosol impacts on clouds and precipitation development in a large winter cyclone. *J. Atmos. Sci.*, **71**, 3636–3658, https://doi.org/10.1175/JAS-D-13-0305.1.

Tuel, A., Y.-W. Choi, D. AlRukaibi, and E. A. Eltahir, 2022: Extreme storms in southwest Asia (Northern Arabian Peninsula) under current and future climates. *Climate Dyn.*, **58**, 1509–1524, https://doi.org/10.1007/s00382-021-05975-7.

Wang, Y., B. Geerts, and C. Liu, 2018: A 30-year convection-permitting regional climate simulation over the interior western United States. Part I: Validation. *Int. J. Climatol.*, **38**, 3684–3704, https://doi.org/10.1002/joc.5527.

Wehbe, Y., D. Ghebreyesus, M. Temimi, A. Milewski, and A. Al Mandous, 2017: Assessment of the consistency among global precipitation products over the United Arab

Emirates. *J. Hydrol.*, **12**, 122–135, https://doi.org/10.1016/j.ejrh.2017.05.002.

——, M. Temimi, D. T. Ghebreyesus, A. Milewski, H. Norouzi, and E. Ibrahim, 2018: Consistency of precipitation products over the Arabian Peninsula and interactions with soil moisture and water storage. *Hydrol. Sci. J.*, **63**, 408–425, https://doi.org/10.1080/02626667.2018.1431647.

Wei, W., R. Zhang, M. Wen, and S. Yang, 2017: Relationship between the Asian westerly jet stream and summer rainfall over central Asia and North China: Roles of the Indian monsoon and the South Asian high. *J. Climate*, **30**, 537–552, https://doi.org/10.1175/JCLI-D-15-0814.1.

——, Q. Ren, M. Lu, and S. Yang, 2022: Zonal extension of the Middle East jet stream and its influence on the Asian monsoon. *J. Climate*, **35**, 4741–4751, https://doi.org/10.1175/JCLI-D-21-0697.1.

Willmott, C. J., and K. Matsuura, 1995: Smart interpolation of annually averaged air temperature in the United States. *J. Appl. Meteor.*, **34**, 2577–2586, https://doi.org/10.1175/1520-0450(1995)034<2577:SIOAAA>2.0.CO;2.

Zhang, F., S. Taraphdar, and S. Wang, 2017: The role of global circumnavigating mode in the MJO initiation and propagation. *J. Geophys. Res. Atmos.*, **122**, 5837–5856, https://doi.org/10.1002/2016JD025665.